

Diffuse X-ray emission around an ultraluminous X-ray pulsar

Andrea Belfiore,^{1,*} Paolo Esposito,^{2,1} Fabio Pintore,¹ Giovanni Novara,² Ruben Salvaterra,¹ Andrea De Luca,^{1,3} Andrea Tiengo,^{2,1,3} Patrizia Caraveo,¹ Felix Fürst,⁴ Gian Luca Israel,⁵ Danilo Magistrali,⁶ Martino Marelli,¹ Sandro Mereghetti,¹ Alessandro Papitto,⁵ Guillermo A. Rodríguez Castillo,⁵ Chiara Salvaggio,^{7,8} Luigi Stella,⁵ Dominic J. Walton,⁹ Anna Wolter,⁸ Luca Zampieri¹⁰

¹*INAF–Istituto di Astrofisica Spaziale e Fisica Cosmica di Milano, via A. Corti 12, 20133 Milano, Italy*

²*Scuola Universitaria Superiore IUSS Pavia, piazza della Vittoria 15, 27100 Pavia, Italy*

³*INFN–Istituto Nazionale di Fisica Nucleare, Sezione di Pavia, via A. Bassi 6, 27100 Pavia, Italy*

⁴*ESAC–European Space Astronomy Centre, Science Operations Department, 28692 Villanueva de la Cañada, Madrid, Spain*

⁵*INAF–Osservatorio Astronomico di Roma, via Frascati 33, 00078 Monteporzio Catone, Italy*

⁶*Universidad Pontificia Comillas Madrid–ICAI, Calle Alberto Aguilera 25, 28015 Madrid, Spain*

⁷*Department of Physics G. Occhialini, University of Milano–Bicocca, piazza dell’Ateneo Nuovo 1, 20126, Milano, Italy*

⁸*INAF–Osservatorio Astronomico di Brera, via Brera 28, 20121 Milano, Italy*

⁹*Institute of Astronomy, University of Cambridge, Madingley Road, Cambridge CB3 0HA, UK*

¹⁰*INAF–Osservatorio Astronomico di Padova, vicolo dell’Osservatorio 5, 35122 Padova, Italy*

*e-mail: andrea.belfiore@inaf.it

Ultraluminous X-ray sources (ULXs) are extragalactic X-ray emitters located off-center of their host galaxy and with a luminosity in excess of a few 10^{39} erg s⁻¹, if emitted isotropically.^{1,2} The discovery of periodic modulation revealed that in some ULXs the accreting compact object is a neutron star,^{3,4,6,7,55} indicating luminosities substantially above their Eddington limit. The most extreme object in this respect is NGC 5907 ULX-1 (ULX1), with a peak luminosity that is 500 times its Eddington limit. During a Chandra observation to probe a low state of ULX1, we detected diffuse X-ray emission at the position of ULX1. Its diameter is 2.7 ± 1.0 arcsec and contains 25 photons, none below 0.8 keV. We interpret this extended structure as an expanding nebula powered by the wind of ULX1. Its diameter of about 200 pc, characteristic energy of ~ 1.9 keV, and luminosity of $\sim 2 \times 10^{38}$ erg s⁻¹ imply a mechanical power of 1.3×10^{41} erg s⁻¹ and an age $\sim 7 \times 10^4$ yr. This interpretation suggests that a genuinely super-Eddington regime can be sustained for time scales much longer than the spin-up time of the neutron star powering the system. As the mechanical power from a single ULX nebula can rival the injection rate of cosmic rays of an entire galaxy,⁸ ULX nebulae could be important cosmic ray accelerators.⁹

NGC 5907 is a nearly edge-on (inclination of 87° [ref.⁵⁶]) spiral galaxy at a distance $D = 17.1$ Mpc [ref.¹¹]. Its source NGC 5907 ULX-1 (henceforth ULX1), with a peak X-ray luminosity $\gtrsim 10^{41}$ erg s⁻¹, is driven by an accreting neutron star with a spin period of ~ 1 s [ref.⁵⁵]. During an X-ray multi-

instrument campaign to study its behavior, ULX1 dimmed its flux by a factor > 50 (Fig. 1) and, on 7 November 2017, Chandra observed the field of ULX1 with its Advanced CCD Imaging Spectrometer for 52 ks. A source at the position of ULX1 was detected at a 7.7σ confidence level (Fig. 2). Since the number of collected photons is rather low, we made extensive use of simulations to assess the robustness of the findings and estimate the parameters characterizing the source. For our analysis, we considered the events between 0.3 and 7.0 keV falling within 3 arcsec from the coordinates of ULX1, totalling 25 photons (3.6 of which are expected from background alone). The emission appears to be extended and indeed we verified that the photon distribution in the detector is not consistent with the point-spread function (PSF) of the telescope: we can reject a point-like nature of this source at the 5σ confidence level. We modelled the emission with a disk profile with uniform surface brightness and estimated the disk radius to be $R_d = 1.35 \pm 0.50$ arcsec. We found no indication of an excess of brightness at the center of the source. To set an upper limit on the flux of ULX1 (the point-like component of the source), we selected the photons in the innermost part of the PSF, within 0.5 arcsec, to compute a Poisson upper limit on the count rate. Assuming a power-law spectrum with photon index $\Gamma = 2$ and an absorbing column $N_H = 5.3 \times 10^{21} \text{ cm}^{-2}$ (the value measured when the source was bright⁵⁵), we obtained an upper limit on the point source unabsorbed flux in the 0.3 – 7.0 keV energy range of $F_X < 3.4 \times 10^{-15} \text{ erg cm}^{-2} \text{ s}^{-1}$ at the 90% confidence level. This corresponds to a limit on the isotropic X-ray luminosity $L_X < 1.2 \times 10^{38} \text{ erg s}^{-1}$, lower than the Eddington luminosity ($L_{\text{Edd}} \sim 1.7 \times 10^{38} \text{ erg s}^{-1}$) for a $1.4-M_\odot$ neutron star.

The diffuse emission at the position of ULX1 can be either an effect of the propagation of the high energy emission of the ULX through a thick dust layer in NGC 5907 or the intrinsic emission of an extended structure physically associated to ULX1. X-ray dust-scattering could produce a halo of the size we observe only if ULX1 were located at least 6 kpc behind the dominant scattering layer. However, in this case, given the high inclination and gas distribution of NGC 5907⁵⁹, standard assumptions imply an X-ray absorption along our line of sight much higher than the column density we derive from the X-ray spectrum of ULX1⁵⁵ (see the Supplementary Information for a discussion and Fig. 6) We therefore concentrate on the hypothesis of nebular emission surrounding the ULX. At the distance of NGC 5907, the radius of the X-ray nebula is $R = 112 \pm 42$ pc. For a collisionally ionized diffuse gas and absorption $N_H = (1.3^{+4.0}_{-1.2}) \times 10^{21} \text{ cm}^{-2}$ we estimate a temperature T corresponding to $k_B T = 1.9^{+2.3}_{-0.8} \text{ keV}$ (where k_B is the Boltzmann constant), an unabsorbed flux $F_X = (6.1^{+6.1}_{-2.5}) \times 10^{-15} \text{ erg cm}^{-2} \text{ s}^{-1}$ and a luminosity $L_X = (2.1^{+2.1}_{-0.9}) \times 10^{38} \text{ erg s}^{-1}$. A diffuse flux consistent with L_{Edd} may suggest that the Eddington-limited radiation from a neutron star is being Compton scattered by the wind. However, given that $\sigma_T \times N_H < 4 \times 10^{-4}$ (where σ_T is the Thompson cross section), $> 99\%$ of the observed emission is unscattered. If this were the remnant of a supernova, its energy would be $E_{sn} > 10^{53} \text{ erg}$ [ref.¹³], corresponding to a hypernova explosion. This is expected to produce a black hole¹⁴ but, in exotic scenarios, it could leave behind a neutron star.¹⁵

Nebular emission has been observed around several ULXs at optical and radio wavelengths.^{1,2,16–20} These nebulae (often referred to as bubbles) are generally attributed to shocks created by outflows from the binary system interacting with the surrounding medium and show some common

traits: diameter of $\sim 200\text{--}400$ pc, expansion speed of $\sim 100\text{--}200$ km s $^{-1}$, characteristic age (derived from the expansion velocity and the size of the nebula) of ~ 1 Myr, and mechanical power $\sim 10^{39}\text{--}10^{40}$ erg s $^{-1}$. Here we explore whether a quasi-isotropic wind shocking the interstellar medium (ISM)^{21,62} can account for the extended X-ray emission around ULX1. As the bubble expands with a radius $R \propto t^{\frac{3}{5}}$ [ref.²¹], the ISM accumulates just behind this external shock. The wind, faster than the shock, also accumulates in another region closer to the source. Assuming that the X-ray emission comes from the outer region, pressure equilibrium at the shock boundary provides an estimate of the shock velocity $v_{\text{sh}} = \sqrt{\frac{5}{16} \frac{k_B T}{m_p}} \simeq 1000$ km s $^{-1}$ (where $k_B T$ comes from the spectral fit and m_p is the proton mass), which entails an age of the bubble $\tau = \frac{3}{5} \frac{R}{v_{\text{sh}}} = (6.7_{-2.8}^{+3.1}) \times 10^4$ yr. This value is much larger than the spin-up timescale of the neutron star that powers the system, 40 yr [ref.⁵⁵]. We also derived an estimate of the ISM density (see Methods) as $n_{\text{ISM}} \simeq 0.08$ cm $^{-3}$ and of the mechanical power carried by the wind, $L_w = (1.3_{-1.0}^{+9.8}) \times 10^{41}$ erg s $^{-1}$, not far from the value of 5×10^{40} erg s $^{-1}$ estimated for the bubble S26 in NGC 7793.^{23,24} If this mechanical power were sustained for $\sim 7 \times 10^4$ yr, then, assuming a typical accretion efficiency onto a neutron star of 17%, $\sim 0.9 M_{\odot}$ should have been accreted to provide enough energy to sustain the nebula. Because the wind carries mechanical power to the nebula, if a large mass has been accreted onto the neutron star, and the mass lost by the system cannot exceed a few $10 M_{\odot}$, then we obtain a speed of the wind $v_w \gtrsim 0.1 c$ where c is the speed of light. This value is consistent with the outflows observed from other ULXs.^{25–27}

NGC 5907 has been observed in H $_{\alpha}$ with the Kitt Peak National Observatory 0.9 m telescope in May 1995.⁶⁰ The high level of contamination from star forming regions and the limited angular resolution (~ 1 arcsec) hamper a detection of a counterpart in H $_{\alpha}$ to the nebula around ULX1. NGC 5907 ULX-1 has been observed in radio at 5 GHz with the Very Large Array in May 2012,⁶¹ detecting no point source down to a flux density of 20 μJy . The radio emission expected from the hot X-ray-emitting plasma is much fainter than this limit (see the Supplementary Information for a discussion). However, because efficient radiative cooling would have boosted the radio emission to ~ 240 μJy [ref.^{63,67}], this limit confirms our adiabatic approximation and justifies the large ratio L_w/L_X .

Observing an X-ray bubble around a ULX requires a number of favourable circumstances: a bubble with the right surface brightness and size to be detectable as extended; a ULX dim enough not to outshine the bubble; a sensitive observation carried out with an instrument with good angular resolution (see the Supplementary Information for a quantitative discussion and Fig. 5). This might explain why no similar structures are commonly observed in association with ULXs (with the notable exception of NGC 7793 S26,²³ which, however, has no associated ULX). Indeed, two follow-up observations with Chandra performed between 2018 February 27 and March 1 for a combined exposure of 50 ks failed to detect the bubble, as ULX1 raised its luminosity to 4×10^{39} erg s $^{-1}$.

The recent discovery of TeV emission from the Galactic microquasar SS 433,⁹ in many ways reminiscent of ULXs,³² suggests that strong shocks associated to ULXs contribute to the cos-

mic ray acceleration. Indeed, the mechanical power of the bubble of ULX1 is comparable to the cosmic-ray injection rate for a whole galaxy.⁸ Since the duty cycle, the lifespan and the population of similar objects are currently poorly known, it is not possible at this stage to quantify their contribution.

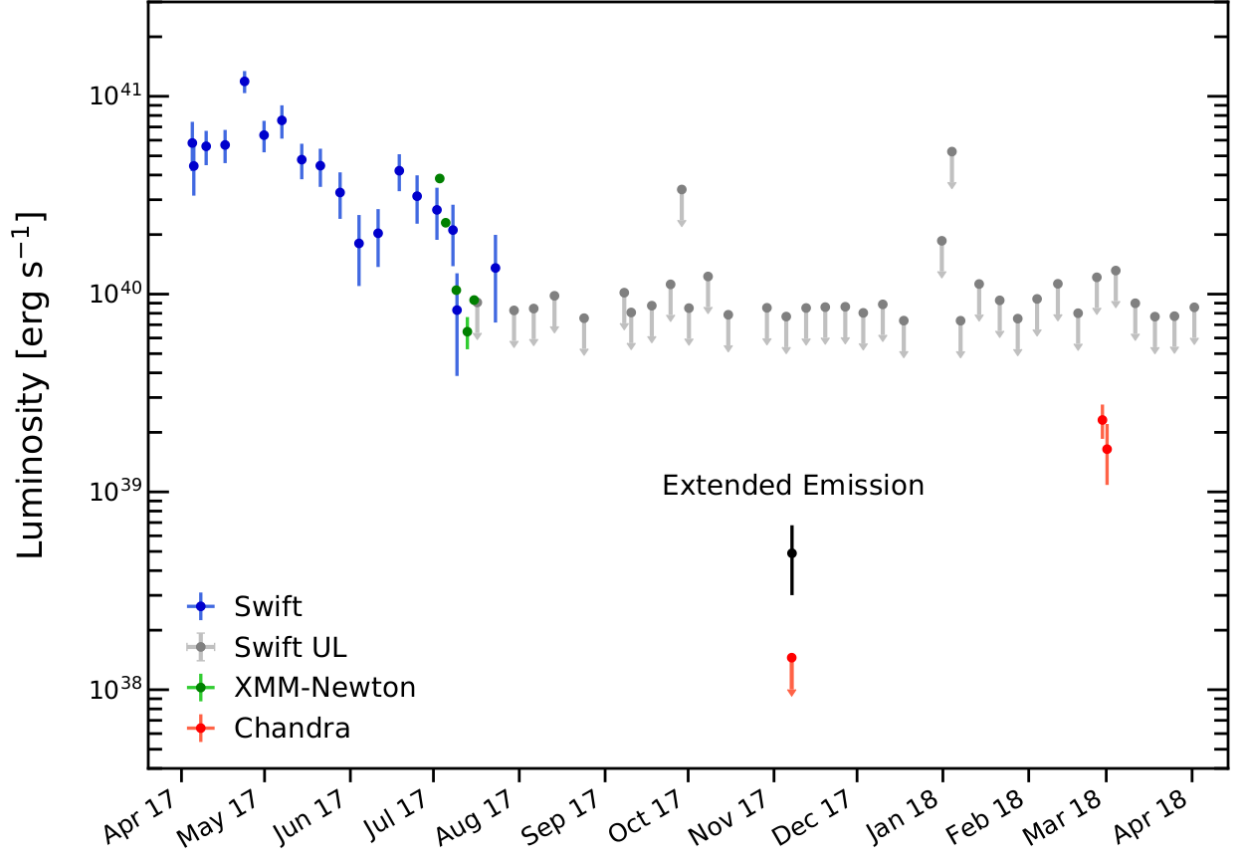


Figure 1: Multi-instrument soft X-ray light curve of NGC 5907 ULX-1 since April 2017, when the Swift monitoring resumed. The y-axis shows the luminosity in the 0.2–10 keV energy range, assuming a distance $D=17.1$ Mpc. In July 2017, when XMM–Newton started observing, the source left its regularly modulated high state⁵⁴. After ULX1 fell below the detection limit of Swift, Chandra observed ULX1 in its low state in November 2017 and obtained an upper limit (red downward arrow), assuming a power-law spectrum with index $\Gamma=2$. The luminosity of the diffuse source (extended X-ray emission) associated to ULX1 assumes a collisional plasma (apec) spectrum with $k_B T = 1.9^{+2.3}_{-0.8}$ keV. The grey arrows and blue points represent Swift upper limits and detections respectively, assuming a broken power law spectrum, as modeled by XMM–Newton in the high state of ULX1.⁵⁵ New Chandra observations (red points) taken in March 2018 found ULX1 in an intermediate state. All the error bars show uncertainties at the 90% confidence level.

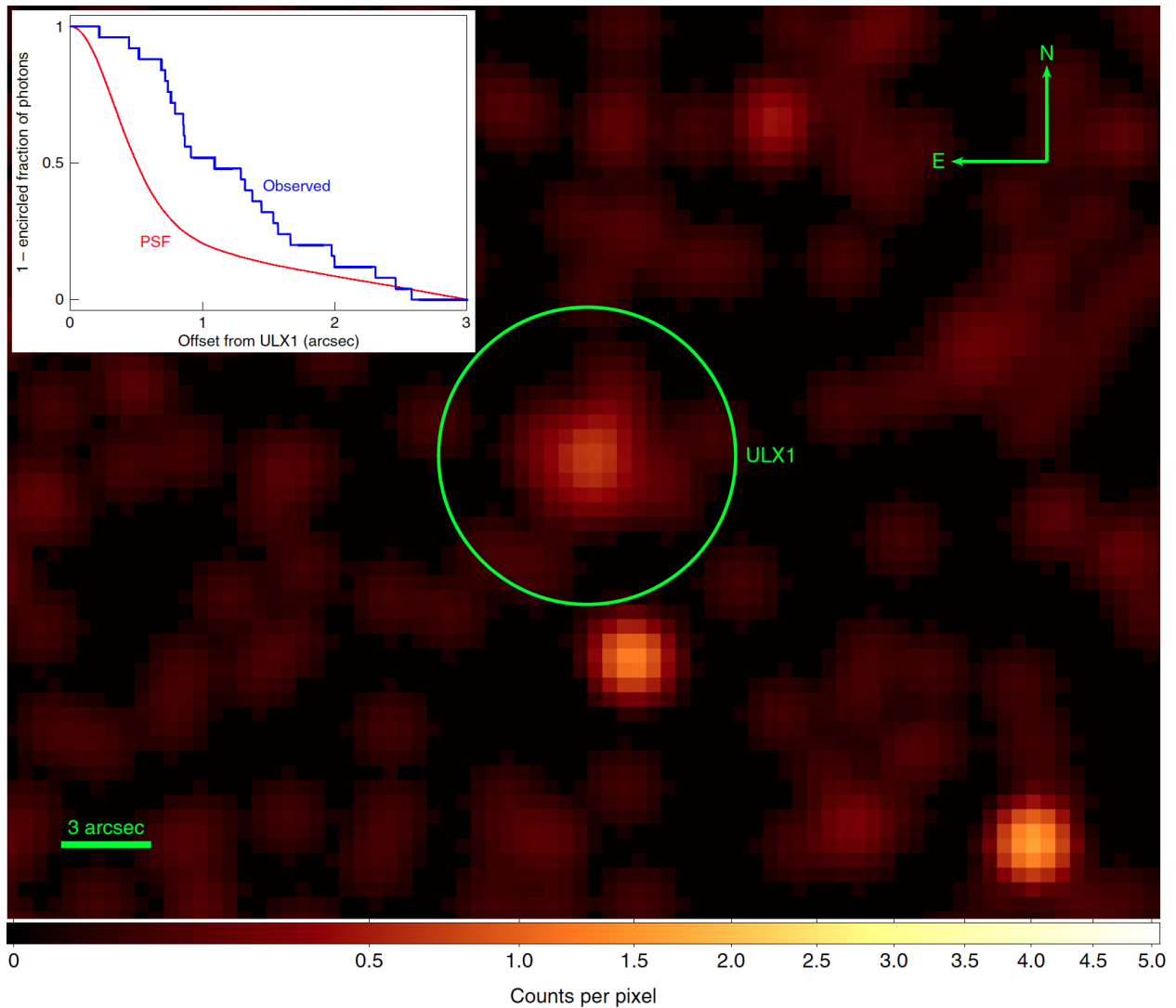


Figure 2: X-ray sky map between 0.3 and 7.0 keV of the region around the direction of NGC 5907 ULX-1 as observed by Chandra in November 2017. Nearby sources are not significantly extended and their radial profile can be compared by eye with that of the diffuse emission. In the latter, no clear enhancement in brightness appears at the center of the source, indicating a discrepancy from the instrument PSF. The green circle, with a radius of 5 arcsec, is centered on the position of ULX1. The scale is in counts per pixel, whose side measures 0.5 arcsec, after smoothing the image through a 2 – D Gaussian kernel with $\sigma_{\text{Gauss}} = 1.5$ pixel. The inset shows a comparison between the PSF (as obtained from simulations, including background) and the observed radial distribution of the events (the y-axis represents the fraction of events falling outside a certain radius). We can reject the hypothesis that the source is point-like with a confidence level of 5σ ($p\text{-value} = 3 \times 10^{-7}$). See Fig. 3 for a broader and unsmoothed version of this map.

References

1. Feng, H. & Soria, R. Ultraluminous X-ray sources in the Chandra and XMM-Newton era. *New Astron. Rev.* **55**, 166–183 (2011).
2. Kaaret, P., Feng, H. & Roberts, T. P. Ultraluminous X-Ray Sources. *ARA&A* **55**, 303–341 (2017).
3. Bachetti, M. *et al.* An ultraluminous X-ray source powered by an accreting neutron star. *Nature* **514**, 202–204 (2014).
4. Fürst, F. *et al.* Discovery of Coherent Pulsations from the Ultraluminous X-Ray Source NGC 7793 P13. *Astrophys. J.* **831**, L14 (2016).
5. Israel, G. L. *et al.* An accreting pulsar with extreme properties drives an ultraluminous x-ray source in NGC 5907. *Science* **355**, 817–819 (2017).
6. Israel, G. L. *et al.* Discovery of a 0.42-s pulsar in the ultraluminous X-ray source NGC 7793 P13. *Mon. Not. R. Astron. Soc.* **466**, L48–L52 (2017).
7. Carpano, S., Haberl, F., Maitra, C. & Vasilopoulos, G. Discovery of pulsations from NGC 300 ULX1 and its fast period evolution. *Mon. Not. R. Astron. Soc.* **476**, L45–L49 (2018).
8. Drury, L. O. . Origin of cosmic rays. *Astroparticle Physics* **39**, 52–60 (2012).
9. Abeysekara, A. U. *et al.* Very-high-energy particle acceleration powered by the jets of the microquasar SS 433. *Nature* **562**, 82–85 (2018).
10. Xilouris, E. M., Byun, Y. I., Kylafis, N. D., Paleologou, E. V. & Papamastorakis, J. Are spiral galaxies optically thin or thick? *Astron. Astrophys.* **344**, 868–878 (1999).
11. Tully, R. B. *et al.* Cosmicflows-2: The Data. *Astron. J.* **146**, 86 (2013).
12. Just, A., Möllenhoff, C. & Borch, A. An evolutionary disc model of the edge-on galaxy NGC 5907. *Astron. Astrophys.* **459**, 703–716 (2006).
13. Blondin, J. M., Wright, E. B., Borkowski, K. J. & Reynolds, S. P. Transition to the Radiative Phase in Supernova Remnants. *Astrophys. J.* **500**, 342–354 (1998).
14. Fryer, C. L. *et al.* Compact Remnant Mass Function: Dependence on the Explosion Mechanism and Metallicity. *Astrophys. J.* **749**, 91 (2012).
15. Barkov, M. V. & Komissarov, S. S. Recycling of neutron stars in common envelopes and hypernova explosions. *Mon. Not. R. Astron. Soc.* **415**, 944–958 (2011). 1012.4565.
16. Pakull, M. W. & Mirioni, L. Optical Counterparts of Ultraluminous X-Ray Sources. In *New Visions of the X-ray Universe in the XMM-Newton and Chandra Era, 26-30 November 2001, ESTEC, The Netherlands*, ArXiv Astrophysics e-prints: astro-ph/0202488 (2002).

17. Pakull, M. W. & Mirioni, L. Bubble Nebulae around Ultraluminous X-Ray Sources. In Arthur, J. & Henney, W. J. (eds.) *Revista Mexicana de Astronomia y Astrofisica Conference Series*, vol. 15 of *Revista Mexicana de Astronomia y Astrofisica*, vol. 27, 197–199 (2003).
18. Pakull, M. W. & Gris e, F. Ultraluminous X-ray Sources: Beambags and Optical Counterparts. In Bandyopadhyay, R. M., Wachter, S., Gelino, D. & Gelino, C. R. (eds.) *A Population Explosion: The Nature & Evolution of X-ray Binaries in Diverse Environments*, vol. 1010 of *American Institute of Physics Conference Series*, 303–307 (2008).
19. Lang, C. C., Kaaret, P., Corbel, S. & Mercer, A. A Radio Nebula Surrounding the Ultraluminous X-Ray Source in NGC 5408. *Astrophys. J.* **666**, 79–85 (2007).
20. Kaaret, P., Corbel, S., Prestwich, A. H. & Zezas, A. Radio Emission from an Ultraluminous X-ray Source. *Science* **299**, 365–368 (2003).
21. Castor, J., McCray, R. & Weaver, R. Interstellar bubbles. *Astrophys. J.* **200**, L107–L110 (1975).
22. Weaver, R., McCray, R., Castor, J., Shapiro, P. & Moore, R. Interstellar bubbles. II - Structure and evolution. *Astrophys. J.* **218**, 377–395 (1977).
23. Pakull, M. W., Soria, R. & Motch, C. A 300-parsec-long jet-inflated bubble around a powerful microquasar in the galaxy NGC 7793. *Nature* **466**, 209–212 (2010).
24. Dopita, M. A., Payne, J. L., Filipovi c, M. D. & Pannuti, T. G. The physical parameters of the microquasar S26 in the Sculptor Group galaxy NGC 7793. *Mon. Not. R. Astron. Soc.* **427**, 956–967 (2012).
25. Pinto, C., Middleton, M. J. & Fabian, A. C. Resolved atomic lines reveal outflows in two ultraluminous X-ray sources. *Nature* **533**, 64–67 (2016).
26. Kosec, P. *et al.* Evidence for a variable Ultrafast Outflow in the newly discovered Ultraluminous Pulsar NGC 300 ULX-1. *Mon. Not. R. Astron. Soc.* **479**, 3978–3986 (2018).
27. Walton, D. J. *et al.* An Iron K Component to the Ultrafast Outflow in NGC 1313 X-1. *Astrophys. J.* **826**, L26 (2016).
28. Rand, R. J. Diffuse Ionized Gas in Nine Edge-on Galaxies. *Astrophys. J.* **462**, 712 (1996).
29. Mezcua, M., Roberts, T. P., Sutton, A. D. & Lobanov, A. P. Radio observations of extreme ULXs: revealing the most powerful ULX radio nebula ever or the jet of an intermediate-mass black hole? *Mon. Not. R. Astron. Soc.* **436**, 3128–3134 (2013).
30. Dopita, M. A. & Sutherland, R. S. Spectral Signatures of Fast Shocks. I. Low-Density Model Grid. *Astrophys. J. Suppl.* **102**, 161 (1996).
31. Caplan, J. & Deharveng, L. Extinction and reddening of H II regions in the Large Magellanic Cloud. *Astron. Astrophys.* **155**, 297–313 (1986).

32. Begelman, M. C., King, A. R. & Pringle, J. E. The nature of SS433 and the ultraluminous X-ray sources. *Mon. Not. R. Astron. Soc.* **370**, 399–404 (2006).
33. Walton, D. J. *et al.* A 78 Day X-Ray Period Detected from NGC 5907 ULX1 by Swift. *Astrophys. J.* **827**, L13 (2016).

#	Mission	Obs.ID	Instrument	Start Date (YYYY-MM-DD)	Total Exposure (ks)
1	Chandra	12987	ACIS-S	2012-02-11	16.0
2	XMM–Newton	0804090301	EPIC	2017-07-02	43.0 (28.0)
3	XMM–Newton	0804090401	EPIC	2017-07-05	39.0 (31.3)
4	XMM–Newton	0804090501	EPIC	2017-07-08	43.0 (34.8)
5	XMM–Newton	0804090701	EPIC	2017-07-12	43.0 (32.5)
6	XMM–Newton	0804090601	EPIC	2017-07-15	40.5 (24.8)
7	Chandra	20830	ACIS-S	2017-11-07	51.3
8	Chandra	20994	ACIS-S	2018-02-27	32.6
9	Chandra	20995	ACIS-S	2018-03-01	16.0

Table 1: **Log of the XMM–Newton and Chandra observations used in this work.** The last column reports the duration of each observation and, for XMM–Newton, in parenthesis, also the net PN exposure, after filtering for background flares.

Methods

X-ray observations and long-term light curve

We consider in this work X-ray observations taken with Chandra, XMM–Newton, and the Neil Gehrels Swift Observatory (see Table 1). Particular care is dedicated to the Chandra observation 20830, taken on 2017 November 6, in which we detected diffuse emission. We used the other data sets to build the long-term light curve of Fig. 1 and/or to improve the astrometry of observation 20830.

Chandra

All Chandra observations we used were carried out with the Advanced CCD Imaging Spectrometer³⁴ (Spectroscopic array, ACIS-S) in full-imaging mode. We used the Chandra Interactive Analysis of Observation (CIAO, v4.10)³⁵ software package and CALDB (v4.7.8). We selected photons in the energy range 0.3–7 keV, and followed the standard analysis threads for data reprocessing, source detection, and flux estimation. We determined the energy boundaries based on the spectral distribution of the ACIS background, which increases significantly outside this band. We defined a circular source region that includes all photons within 3 arcsec from the direction of ULX1. This radius, which contains 98.5% of the PSF, limits the contamination from background and other sources, but is large enough to make it possible to appreciate the main features of the X-ray source. We defined an annular background region centered at the location of ULX1, with radii 10 arcsec and 30 arcsec. We removed from this region circles with radii of 5 arcsec around each other source, and a circle with radius of 10 arcsec around NGC 5907 ULX-2, being particularly bright at the time. For observation 20830, these criteria leave 25 photons in the source region and 277 photons in the background region, corresponding to 3.6 background photons expected in the source region (see Fig. 3).

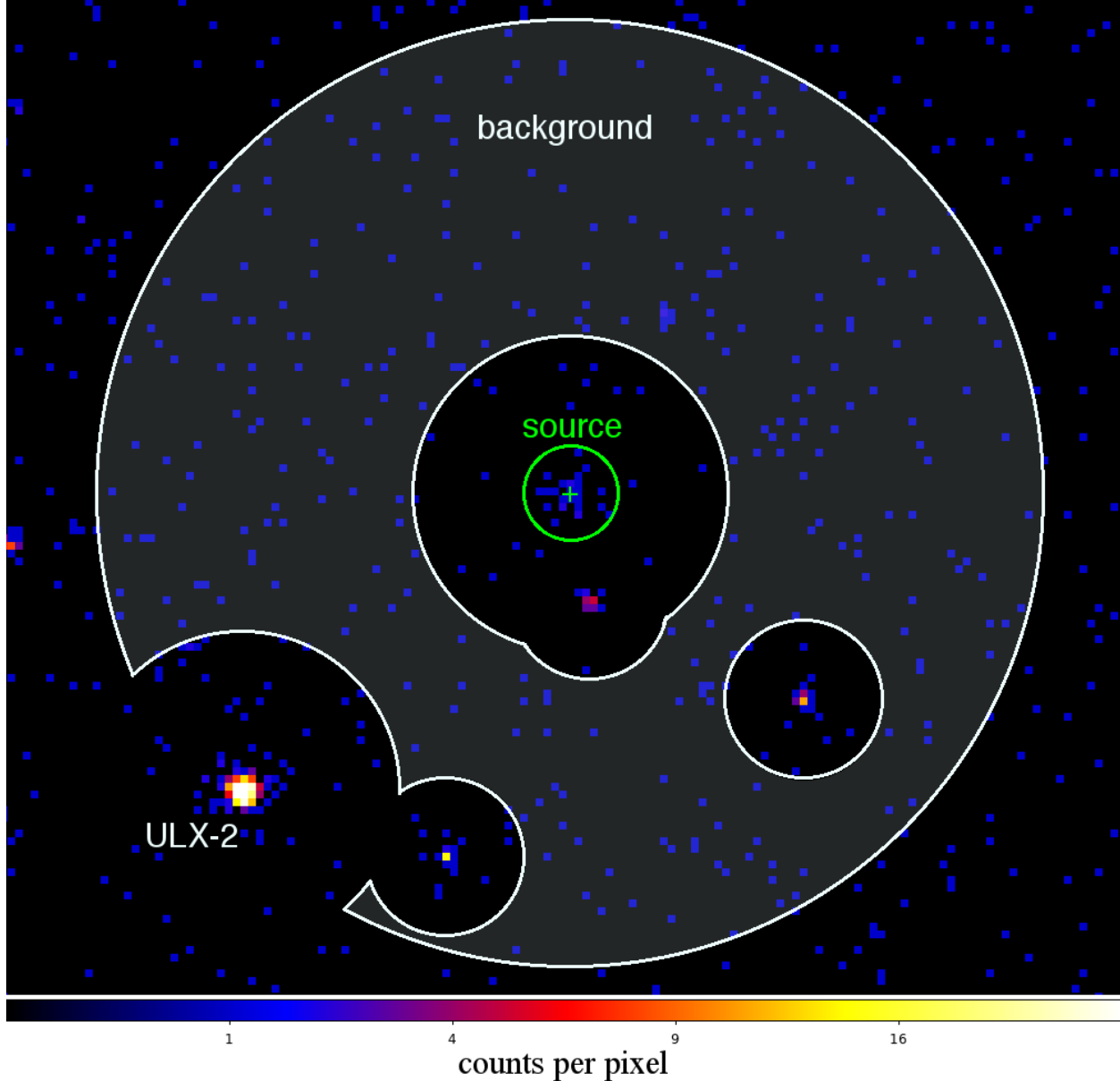


Figure 3: Counts map between 0.3 and 7.0 keV from the Chandra observation of November 2017 (Obs. Id. 20830), centered on the direction of ULX1. ULX1 is marked here by a green cross. The green circle represents the source extraction region and contains 25 photons. The white shaded area covers the region used to estimate the background level and contains 277 photons. It is shaped as an annulus centered on ULX1 from which circles around each source have been removed. We expect a background contamination of 3.6 photons in the source region. The bright source in the bottom left corner is NGC 5907 ULX2.

XMM–Newton

In the XMM–Newton observations, the positive–negative junction³⁶ (pn) and the two metal oxide semi-conductor³⁷ (MOS) CCD cameras of the EPIC instrument were all operated in Full Frame mode. We used the XMM–Newton Science Analysis Software³⁸ (SAS) v14.5 for data reduction. After removing intervals of high background, we selected the events setting FLAG==0 and PATTERN<=4 and PATTERN<=12 for pn and MOS, respectively. We extracted the source spectra and event lists from a circular region with radius 30 arcsec around the best-fit Chandra source position, RA = 228.994289° and Dec = 56.302851° (J2000), in the energy range 0.3–10 keV. We estimated the background from a circular region with radius 65 arcsec, close to ULX1 but free of sources, for each observation. We excluded from our analysis the XMM–Newton observation 0795712601 as source contamination, mainly from NGC 5907 ULX-2 but also from other sources in NGC 5907, undermines a clear characterization of ULX1.³⁹

We simultaneously analysed all XMM–Newton spectra in the energy range 0.3–10 keV and we fitted them with an absorbed broken power law model (bknpow in XSPEC⁴⁰). The Tuebingen-Boulder ISM absorption model (tbabs) was adopted and the abundances were set to those of ref.⁴¹. We fixed the values of the break energy and the high-energy spectral index, to those obtained in ref.⁵⁵, ($E_b = 6.7$ keV and $\Gamma_2 = 2.9$), as they were better constrained including NuSTAR data and consistent with all the XMM–Newton observations of ULX1 in a high state. We also fixed the column density to the best-fit value in ref.⁵⁵, $N_H = 5.3 \times 10^{21}$ cm⁻². We left free to vary the low-energy photon index and the normalization. We obtained an acceptable fit ($\chi^2_\nu = 1.12$ for 439 degrees of freedom), with low-energy photon indices of $\Gamma_1^{(2)} = 1.72 \pm 0.03$, $\Gamma_1^{(3)} = 1.88 \pm 0.04$, $\Gamma_1^{(4)} = 1.90 \pm 0.06$, $\Gamma_1^{(5)} = 2.82 \pm 0.18$, and $\Gamma_1^{(6)} = 2.08 \pm 0.07$ for the five observations, in chronological order (the superscripts refer to the observation codes in Table 1). The resulting 0.3–10 keV unabsorbed fluxes are $F_X^{(2)} = (7.09 \pm 0.15) \times 10^{-13}$ erg cm⁻² s⁻¹, $F_X^{(3)} = (4.22 \pm 0.10) \times 10^{-13}$ erg cm⁻² s⁻¹,

$F_X^{(4)} = (1.92 \pm 0.07) \times 10^{-13}$ erg cm⁻² s⁻¹, $F_X^{(5)} = (9.2 \pm 1.2) \times 10^{-14}$ erg cm⁻² s⁻¹, and $F_X^{(6)} = (1.65 \pm 0.07) \times 10^{-13}$ erg cm⁻² s⁻¹ (see Fig. 1). All these uncertainties are at the 90% confidence level. A careful spectral characterization, to be compared with other spectral analyses in the literature, goes beyond the scope of this paper.

Swift

The X-Ray Telescope⁴² (XRT) on board Swift uses a CCD detector sensitive to photons with energies between 0.2 and 10 keV. All observations analyzed in this work were performed in imaging photon counting (PC) mode. We used FTOOLS⁴³ v6.15 for standard data processing. We extracted the source events within a radius of 20 arcsec from the Chandra position of ULX1, and evaluated the background in a source-free circular region of radius 130 arcsec, avoiding the plane of NGC 5907. The ancillary response files generated with xrtmkarf account for different extraction regions, vignetting and point-spread function corrections. We used the latest available spectral redistribution matrix (v014). We converted the source rate to 0.2–10 keV luminosity by assuming a distance $D = 17.1$ Mpc and an absorbed broken power-law spectral model with indices 1.57 and 2.87, and break energy 6.42 keV. These are the best-fit parameters obtained in the high state of

ULX1,⁵⁵ consistent with, but more constrained, than the values obtained in the spectral analysis described in the previous section.

As the region around ULX1 is rich of X-ray sources from NGC 5907, which Chandra can resolve but Swift cannot, XRT observations are likely affected by source contamination. A dedicated analysis that addresses this issue is not straightforward and goes beyond the scope of this paper.

Analysis of the Chandra observation of diffuse emission around ULX1

Relative astrometry

We considered Chandra observations 12987 and 20994, besides observation 20830. We reprocessed the data, extracted images, and run the CIAO task `wavdetect`, following the indications in the Chandra analysis threads. We selected the sources within 1 arcmin from the nominal position of ULX1, excluding ULX1 itself. We found the translations that best map the coordinates of the sources in observations 12987 and 20994 to those in observation 20830, using the CIAO task `wcs_match`. We applied these corrections (measuring 0.13 arcsec and 0.30 arcsec, respectively) to the images and aspect solutions of observations 12987 and 20994 and launched again the task `wavdetect`. The localization of ULX1 in the two observations is now compatible within 1σ in RA ($|\Delta\text{RA}| = 0.06$ arcsec) and Dec ($|\Delta\text{Dec}| = 0.06$ arcsec), in the relative frame of observation 20830. Therefore, we take the barycenter of these two positions as the (J2000) nominal position of ULX1: RA = $228.994289(8)^\circ$ and Dec = $56.302851(4)^\circ$ (or RA = $15^{\text{h}}15^{\text{m}}58^{\text{s}}.63$, Dec = $+56^\circ18'10''.3$). The best fit coordinates of the closest source to ULX1 in observation 20830 are: RA = $228.99414(11)^\circ$ and Dec = $56.30284(6)^\circ$ (J2000). These two positions are compatible within 2σ , being offset by 0.3 arcsec, with a 1σ uncertainty of 0.21 arcsec. Therefore, we identify the source in observation 20830 with ULX1 and adopt the nominal position of ULX1 in the analysis that follows.

Extension

A first indication of source extension comes from the output of the CIAO tool `wavdetect`. We tested for and measured the extension of our source, by studying its radial brightness profile. We used a Kolmogorov–Smirnov test, which quantifies the goodness of fit by measuring the maximum absolute difference between the cumulative distribution of observed events and the model. To take into account the complex shape of the PSF and other effects due to the spacecraft dithering, we simulated with MARX⁴⁴ (v5.3.3) a large number of events associated to a point source with characteristics similar to ULX1 in observation 20830, including its position on the detector. In order to avoid photon pileup, which alters the PSF, we generated 50 realizations of a source with 1000 events and combined them. We assumed an absorbed ($N_{\text{H}} = 5.3 \times 10^{21} \text{ cm}^{-2}$, the value measured for ULX1 in the high state⁵⁵), power-law ($\Gamma = 2$) spectrum and a direction consistent with those of ULX1. We obtain consistent results assuming the best-fit thermal bremsstrahlung spectral model described in the next section. We generated a number of simulated background events, drawing from a two-dimensional uniform distribution.

We extracted the observed cumulative distribution of events within a radius R from the source

center. We used the nominal direction of ULX1 obtained through astrometric analysis (see the previous section), but using the observed centroid does not alter our results. For the simulated point source, we included the expected uniform background contribution. We applied the same selection criteria to the simulated data set and considered only photons in the source region (with radius 3 arcsec): 25 observed photons compared against 4×10^4 simulated photons.

A Kolmogorov–Smirnov test finds a maximum difference between the two cumulative radial distributions, $D=0.525$ (see Fig 2). This implies that the source associated to ULX1 is not point-like with a confidence level of 5σ (p-value = 3×10^{-7}). We repeated the same analysis simulating extended sources with a disk profile of uniform surface brightness. We can reject at the 2σ confidence level all values of the disk radius outside the range $R_d = 1.35 \pm 0.50$ arcsec. We repeated the same analysis assuming a smooth halo shape⁵³ with a hole, as described in the section of the Supplementary Material where we apply a dust scattering model. We constrained the values of the distance between the source and a dust layer to $d_{sd} = 11 \pm 5$ kpc. In the spirit of reproducible results, we provide the code of the MARX plugin (Draine_halo.c) that we used to simulate such a dust halo at <https://github.com/andrea-belfiore/MARX-plugins.git>.

Spectral analysis

We analysed the spectrum of the extended source with XSPEC, adopting a collisional plasma model (apec), absorbed according to the Tübingen-Boulder absorption model (tbabs) and set the abundances to those of ref.⁴¹. As the number of events is very low, we used C-statistics⁴⁶ and verified through Monte Carlo simulations similar to those described above, that we obtain identical estimates and error bars. All the uncertainties are stated at 90% CL. The absorption column is poorly constrained by the data (see Fig. 4), but physical constraints are given by the absorption level of our Galaxy in the direction of ULX1, $N_{H,G} = 1.2 \times 10^{20} \text{cm}^{-2}$, and the absorption measured in the high state of ULX1, $N_{H,U} = 5.3 \times 10^{21} \text{cm}^{-2}$ (that includes internal absorption by the ULX itself). We repeated the same analysis adopting the best-fit value $N_H = 1.3 \times 10^{21} \text{cm}^{-2}$, that provided us with the best-fit estimates for all parameters, and for the two extreme values $N_{H,G}$ and $N_{H,U}$ that determine our uncertainties (that cover the 90% CL error bars for all allowed values of N_H).

We estimate a characteristic energy $k_B T = 1.9_{-0.8}^{+2.3}$ keV, a normalisation $N = 3.5_{-1.9}^{+2.5} \times 10^{-6}$, and an unabsorbed 0.3-7.0 keV flux $F_X = 6.1_{-2.5}^{+6.1} \times 10^{-15} \text{erg cm}^{-2} \text{s}^{-1}$, corresponding to an isotropic 0.3-7.0 keV luminosity $L_X = 2.1_{-0.9}^{+2.1} \times 10^{38} \text{erg s}^{-1}$.

We also tested through Monte Carlo simulations a dust-scattering spectrum expected from the model outlined in a following section. This model is acceptable at the 2σ level (the spectrum changes so slightly with the tuning parameters that we cannot constrain them in this way).

We try to estimate the flux of a point-like component associated to ULX1. To this aim, we consider only the innermost photons, within 0.5 arcsec from the location of ULX1, determined

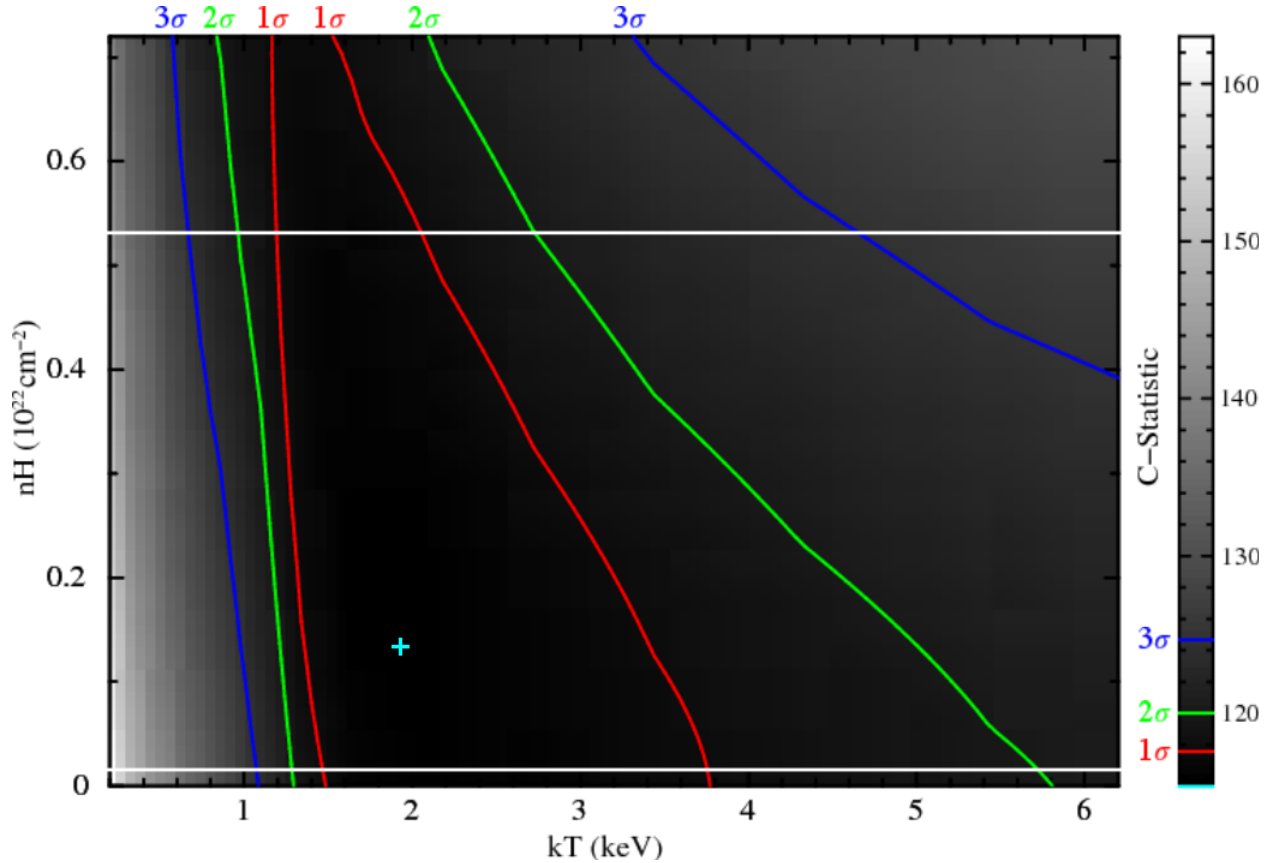


Figure 4: Joint spectral fit to the plasma temperature and the absorption column obtained with Xspec and an apec model, of the extended emission observed with Chandra in November 2017 (Obs. Id. 20830). The cyan cross corresponds to the best fit on these X-ray data. The red, green, and blue color contours indicate the 1, 2, and 3σ confidence levels, respectively. Although the column density is poorly constrained by these X-ray data, we have two external constraints, marked as horizontal white lines in this plot. The lower value, $N_{\text{H,G}} = 1.2 \times 10^{20} \text{cm}^{-2}$, is given by the Galactic absorption in the direction of ULX1. The higher value $N_{\text{H,U}} = 5.3 \times 10^{21} \text{cm}^{-2}$, was estimated in the high state of ULX1, and thus might include internal absorption.

as described in the astrometry section. We assume for the point source a power-law spectrum with $\Gamma=2$ and the absorption column $N_{H,U} = 5.3 \times 10^{21} \text{cm}^{-2}$ measured for ULX1 in its high state. We used the CIAO tool `srcflux`, that applies an aperture photometry, taking into account the response of the instrument, the encircled fraction (fraction of the PSF within each region), statistical uncertainties, position on the detector, and other effects. It provides an upper limit on the flux (at the 90% confidence level) of $F_X < 3.4 \times 10^{-15} \text{erg cm}^{-2} \text{s}^{-1}$. This corresponds to a luminosity $L_X < 1.2 \times 10^{38} \text{erg s}^{-1} = 0.68 L_{14}$, where $L_{14} = 1.764 \times 10^{38} \text{erg s}^{-1}$ is the Eddington limit for a $1.4-M_\odot$ neutron star.

Physical modeling of the expanding nebula

We assume that an isotropic wind with constant power L_w is emitted from the ULX system, shocks the external medium (ISM) and expands according to a self-similar solution.^{21,62} After a short free expansion period, the wind forms a shock that starts as adiabatic but becomes more and more radiatively efficient. In this phase, the expanding nebula (bubble) is radially structured in 4 regions:

1. Close to the source is the low-density left-over of the swept up ISM, where the wind expands freely (free wind region);
2. Starting at a radius R_1 the wind, faster than the shock, accumulates, increasing density and temperature (shocked wind region);
3. Starting at a radius R_c the swept up ISM accumulates, increasing density and temperature (shocked ISM region);
4. Beyond a radius R_2 the ISM is still unperturbed by the shock (ISM region).

In this model, there are two shocked regions where X-rays could be emitted: the shocked wind region and the shocked ISM region. The first scenario was considered in a set of simulations⁴⁷ of expanding nebulae, and, with the boundary conditions set in these simulations, it cannot reach an X-ray luminosity larger than $\sim 10^{35} \text{erg s}^{-1}$. Either this scenario is missing some dominant effect, or it can be ruled out in the context of ULX1; we explore here the other scenario.

If we assume that the X-rays are produced in the shocked ISM region, then the observed disk radius $R_d = 1.35 \pm 0.50 \text{arcsec}$ coincides with $R_2(\tau) = 112 \pm 42 \text{pc}$ at a distance $D = 17.1 \text{Mpc}$, where τ is the current age of the bubble. Strong shock conditions for the temperature of the shocked ISM provide a direct estimate of the current speed of the shock v_{sh} :

$$v_{\text{sh}}^{(0)} = \sqrt{\frac{16}{3} \frac{kT}{m_p}} = (3.3_{-0.8}^{+1.6}) \times 10^{-3} c = (9.9_{-2.4}^{+4.8}) \times 10^2 \text{km s}^{-1} \quad (1)$$

Because observations of other nebulae show that the shock speed is somewhat overestimated with this approximation, we introduce a factor $\xi < 1$ that accounts for this discrepancy: $v_{\text{sh}} = v_{\text{sh}}^{(0)} \times \xi$.

A standard bubble model, with a constant injection of mechanical power L_w in a uniform ISM with density $n_{\text{ISM}} = n_1 \times \text{cm}^{-3}$, predicts a time dependence of the bubble size:

$$R_2(t) = \alpha \left(\frac{L_w t^3}{n_{\text{ISM}} m_p} \right)^{1/5} \quad (2)$$

where $\alpha = 0.88$ is a numerical constant.⁶²

Under these assumptions, as $v_{\text{sh}} = \frac{dR_2}{dt}$, we can estimate the age of the bubble:

$$\tau = \frac{3 R_2}{5 v_{\text{sh}}} = (6.7^{+3.1}_{-2.8}) \times 10^4 \text{ yr} \times \xi^{-1} \quad (3)$$

As v_{sh} largely exceeds the sound speed in the ISM, the Rankine–Hugoniot conditions at the shock front grant that the plasma density just inside the shocked region is $n_{\text{sh}} = W \times n_{\text{ISM}}$, with a compression factor $W \simeq 4$. However, as a high radiative efficiency strongly increases this value, we maintain it as a free parameter. According to the standard bubble model, n_{sh} decreases down to 0 as the radial distance r approaches a contact discontinuity at $r = R_c$. Because the bremsstrahlung emissivity $\epsilon \propto n_{\text{sh}}^2$, we assume that most emission is produced close to R_2 . We estimate the size of this emitting region V_{sh} by assuming that it contains most of the swept up material from the ISM:

$$V_{\text{sh}} \simeq \frac{4}{3} \pi R_2^3 \frac{n_{\text{ISM}}}{n_{\text{sh}}} = (1.5^{+2.3}_{-1.1}) \times 10^6 \text{ pc}^3 \times \left(\frac{W}{4} \right)^{-1} \quad (4)$$

We can now extract from the normalisation of the apc model an estimate of the shocked plasma density as

$$n_{\text{sh}} = 3.1^{+11}_{-2.1} \times 10^{-1} \text{ cm}^{-3} \times \left(\frac{W}{4} \right)^{\frac{1}{2}} \quad (5)$$

This value is broadly consistent with those observed in optical/radio ULX bubbles.²³

We use eq. (2) to provide an estimate of the mechanical power of the wind L_w :

$$L_w = \frac{m_p n_{\text{ISM}} R_2^5}{\alpha^5 \tau^3} \simeq 108 m_p n_{\text{ISM}} R_2^2 \left(\frac{k_B T}{m_p} \right)^{3/2} \times \xi^3 = (1.3^{+9.8}_{-1.0}) \times 10^{41} \text{ erg s}^{-1} \times \xi^3 \times \left(\frac{W}{4} \right)^{-\frac{1}{2}} \quad (6)$$

where we used eqq. (3) and (1) and our estimates for R_d , $k_B T$, and n_{ISM} , leading to large uncertainties. This value is in the same order of magnitude as the X-ray luminosity observed from ULX1 at its peak, if emitted isotropically.⁵⁵ Although L_w is weakly constrained from our results, we deem it extremely unlikely that it can be much higher.

Indeed, if we suppose that ULX1 sustained this value of L_w for the age of the nebula τ , its wind would have carried an energy $E = L_w \tau = (2.8^{+18}_{-2.2}) \times 10^{53} \text{ erg} \times \xi^2 \times \left(\frac{W}{4} \right)^{-\frac{1}{2}}$. As the wind,

and therefore the bubble, is powered by accretion onto a neutron star, the accreted mass must be at least:

$$M_{\text{accr}} = \frac{E}{\eta c^2} \simeq (1.8_{-1.5}^{+12}) \times 10^{33} \text{ g} = 0.9_{-0.7}^{+5.9} M_{\odot} \quad (7)$$

where $\eta \simeq \frac{GM_{ns}}{R_{ns}c^2} \simeq 17\%$ is the accretion efficiency of a neutron star with mass $M_{ns} = 1.4M_{\odot}$ and radius $R_{ns} = 12 \text{ km}$. The best-fit value of M_{accr} might be too large for a neutron star, as it would have probably already collapsed into a black hole, but a value of $M_{\text{accr}} < 0.5 M_{\odot}$ is more plausible. As the accretion power is not all channelled into the wind, but must also sustain the luminosity of ULX1, it seems likely that our simple model might need some revision.

We can relate the total mass ejected by the wind, M_w to E and, indirectly, to M_{accr} :

$$M_w = \frac{2\eta M_{\text{accr}} c^2}{v_w^2} \quad (8)$$

where v_w is the speed of the wind. If we assume $M_{\text{accr}} \simeq 0.5 M_{\odot}$, then, to keep $M_w \lesssim 10M_{\odot}$ as expected for an X-ray binary system, $v_w > 0.1 c$. This value of v_w agrees with the velocity measured in outflows from various ULXs.²⁵⁻²⁷

References

34. Garmire, G. P., Bautz, M. W., Ford, P. G., Nousek, J. A. & Ricker, G. R., Jr. Advanced CCD imaging spectrometer (ACIS) instrument on the Chandra X-ray Observatory. In Truemper, J. E. & Tananbaum, H. D. (eds.) *X-Ray and Gamma-Ray Telescopes and Instruments for Astronomy*, vol. 4851 of *Proceedings of the SPIE*, 28–44 (SPIE, Bellingham, 2003).
35. Fruscione, A. *et al.* CIAO: Chandra’s data analysis system. In Silva, D. R. & Doxsey, R. E. (eds.) *Observatory Operations: Strategies, Processes, and Systems*, vol. 6270 of *SPIE Conference Series*, 62701V (SPIE, Bellingham, 2006).
36. Strüder, L. *et al.* The European Photon Imaging Camera on XMM-Newton: The pn-CCD camera. *Astron. Astrophys.* **365**, L18–L26 (2001).
37. Turner, M. J. L. *et al.* The European Photon Imaging Camera on XMM-Newton: The MOS cameras. *Astron. Astrophys.* **365**, L27–L35 (2001).
38. Gabriel, C. *et al.* The XMM-Newton SAS - Distributed Development and Maintenance of a Large Science Analysis System: A Critical Analysis. In Ochsenbein, F., Allen, M. G. & Egret, D. (eds.) *Astronomical Data Analysis Software and Systems (ADASS) XIII*, vol. 314 of *ASP Conf. Ser. (San Francisco, CA: ASP)*, 759 (2004).
39. Pintore, F. *et al.* A new ultraluminous X-ray source in the galaxy NGC 5907. *Mon. Not. R. Astron. Soc.* **477**, L90–L95 (2018).

40. Arnaud, K. A. XSPEC: The First Ten Years. In Jacoby, G. H. & Barnes, J. (eds.) *Astronomical Data Analysis Software and Systems V*, vol. 101 of *Astron. Soc. Pac. Conf. Series*, 17–20 (1996).
41. Wilms, J., Allen, A. & McCray, R. On the Absorption of X-Rays in the Interstellar Medium. *Astrophys. J.* **542**, 914–924 (2000).
42. Burrows, D. N. *et al.* The Swift X-Ray Telescope. *Space Science Reviews* **120**, 165–195 (2005).
43. Blackburn, J. K. FTOOLS: A FITS Data Processing and Analysis Software Package. In Shaw, R. A. and Payne, H. E. and Hayes, J. J. E., eds., *Astronomical Data Analysis Software and Systems IV*, vol. 77 of *Astron. Soc. Pac. Conf. Series*, 367 (1995).
44. Davis, J. E. *et al.* Raytracing with MARX: x-ray observatory design, calibration, and support. In *Space Telescopes and Instrumentation 2012: Ultraviolet to Gamma Ray*, vol. 8443 of Proc. SPIE, 84431A (SPIE, Bellingham, 2012).
45. Draine, B. T. Scattering by Interstellar Dust Grains. II. X-Rays. *Astrophys. J.* **598**, 1026–1037 (2003).
46. Cash, W. Parameter estimation in astronomy through application of the likelihood ratio. *Astrophys. J.* **228**, 939–947 (1979).
47. Siwek, M., Sądowski, A., Narayan, R., Roberts, T. P. & Soria, R. Optical and X-ray luminosities of expanding nebulae around ultraluminous X-ray sources. *Mon. Not. R. Astron. Soc.* **470**, 361–371 (2017).

Supplementary Information

Detectability of similar features

We explore the conditions under which an extended feature associated to a point source, particularly a ULX, is detectable. Due to the small angular scale of such a feature, we restrict our scope to Chandra, which provides the best angular resolution among the currently operating X-ray observatories. We simulate with MARX a large number of extended sources overlapping a point source and a uniform background, scanning a broad range for each parameter: the size (disk radius R_d) and the fluence of the extended source, the fluence of the point source (N_p) and that of the background. We assume for the extended source a uniform disk shape and a bremsstrahlung spectrum with $kT = 0.76$ keV, and for the point source a power-law spectrum with index $\Gamma = 2$.

By scanning over the fluence of the extended source, we determine for each configuration of the other parameters the number of photons N_{90} that are needed from the extended source to detect it as extended with a 90% probability. We consider a source detected as extended if we can reject at the 3σ confidence level the hypothesis that the source is point-like, if we apply a procedure identical to the one we applied to the source associated to ULX1. It turns out that the background level has an appreciable impact only in those cases where the number of events from the two source components (one point-like, the other extended) combined is very small. Therefore, we fix the number of expected background photons within 3 arcsec to 4, close to the value we estimate in the field of ULX1. We also find that fixing N_p and increasing R_d , N_{90} decreases down to a minimum value for $R_d \gtrsim 2$ arcsec.

The left hand panel of Suppl. Fig. 5 shows N_{90} as a function of N_p for a relatively large source, with $R_d \gtrsim 2$ arcsec. For a feature similar in physical size as the one we detect around ULX1, this corresponds to a distance of the host galaxy $\lesssim 12$ Mpc. We overplot a few lines indicating fixed count ratios between the point source and the extended source. If we assume that the brightness of the extended feature is constant, the blue and cyan lines correspond to the counts ratios that we expect when ULX1 is in its high state, the green line the counts ratio in the intermediate state, and the red line the counts ratio in the low state. The left hand panel of Suppl. Fig. 5 shows that a ULX must be in a low state for us to be able to detect a dim extended feature associated to it, even if the source is not too far from us.

Then, we assume that the extended source is 5 times more luminous than the point source (reproducing the off state of a transient ULX) and check its detectability at larger distance $\gtrsim 10$ Mpc. We consider a 50 ks Chandra observation and the same physical size for the extended feature as the one we detect around ULX1. The right hand panel of Suppl. Fig. 5 shows the luminosity of the extended feature (L_{90}) corresponding to N_{90} as a function of the distance of the host galaxy. If we assume that the X-ray luminosity of the nebula should be lower than a few 10^{39} erg s^{-1} , then we can only appreciate the extension of sources within ~ 20 Mpc (and only when the point source

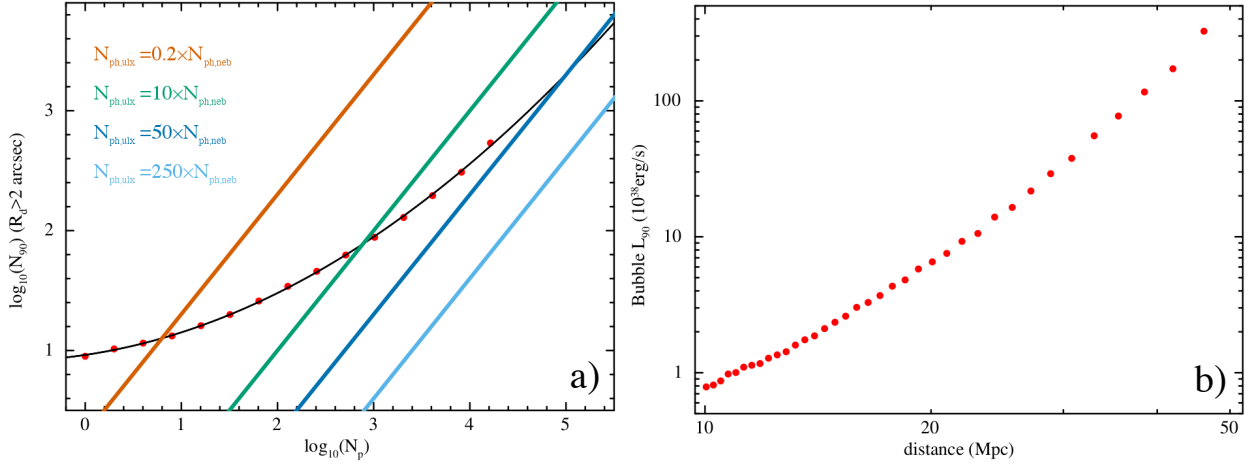


Figure 5: Detectability of a ULX nebula with Chandra. a): Minimum number of photons from a sufficiently extended source ($R_d \gtrsim 2$ arcsec), on top of a point source, for it to appear extended. This value grants a 90% probability of rejecting at the 3σ confidence level the hypothesis that the source is point-like. The axes report the base-10 logarithms of counts in the point-like (x-axis) and extended (y-axis) components. Straight lines indicate a fixed ratio of counts between the two components. Only if the point-like component is much dimmer than the extended component, the extended feature can be detected. **b):** Minimum luminosity of an extended feature to be detected as a function of the distance of its host galaxy. The spectra of the components, their relative flux ratio, and physical size of the extended component are fixed to the best-fit values for NGC 5907 ULX-1. A feature dimmer than 7×10^{39} erg s $^{-1}$ can be detected only within 20 Mpc.

is in a very low state). Very few currently known ULXs are eligible,⁴⁸ and they should be closely monitored, because only when they are in a low state Chandra could probe with a long stare if they share a feature similar to the one we observe in ULX1 in this paper.

Application of a dust scattering model

We investigated the possibility that the extended emission around ULX1 is due to X-ray dust-scattering, as sometimes it is observed for X-ray sources whose emission passes through clouds of dust (e.g. refs. ^{49–51}). The observed angular deviation ϕ is related⁵² to the scattering angle θ and to the source and dust distances (D and D_d , respectively) by $\phi \simeq (1 - x) \times \theta$, where $x = D_d/D$. For dust located in our Galaxy and not too close to the X-ray source (since the X-ray scattering cross section rapidly drops with the scattering angle), we can see scattering halos around X-ray sources up to dozens of arcmin. An extended X-ray scattering halo by extragalactic dust, instead, has never been detected because for $x \approx 1$, the uncertainty in the PSF hampers a measure of the tiny extent of these halos. However, the favourable combination of the Chandra PSF, the edge-on orientation of NGC 5907, the extreme luminosity of ULX1, and its abrupt switch-off, might have given us the opportunity to resolve spatially—for the first time—the X-ray emission from an extragalactic compact object that was scattered by the dust in its host galaxy.

In fact, we can interpret the halo we saw as due to the photons emitted during the high state of ULX1 and scattered in our direction by the interstellar dust in its host-galaxy, the difference between the two optical paths causing a delay. Indeed, dust in NGC 5907 prevents us to see any optical counterpart to ULX1, even with the high sensitivity of the Hubble Space Telescope. In the following section, we apply the X-ray scattering model to our system and check its consistency.

As a first approximation, we assume that the dust is uniformly distributed in a thin wall at a distance $d_{sd} = (1 - x) \times D = d_{10} \times 10$ kpc from ULX1, where $D = 17.1$ Mpc is the distance of NGC 5907. The difference in optical path with respect to a photon reaching us directly causes a delay:

$$\Delta t(x, \phi) \simeq \frac{d_{sd} ((1 - x)\theta^2 + \phi^2)}{2c(1 - x)} \simeq \frac{D\phi^2}{2c(1 - x)}. \quad (9)$$

The brightness profile of the halo can be expressed⁵² as:

$$B_h(x, t, \phi) = N_d L_{src} (t - \Delta t(x, \phi)) \int S(E) \frac{d\sigma}{d\theta} \left(\frac{\phi}{1 - x}, E \right) dE, \quad (10)$$

where N_d is the dust (scattering centers) column density, L_{src} is the X-ray luminosity of the source, $S(E)$ is the spectral energy distribution of the source normalized to 1, and $\frac{d\sigma}{d\theta}$ is the differential scattering cross-section.

If L_{src} switches on at an epoch t_{on} , then, according to eqq. (10) and (9), a halo forms up to a radius:

$$\phi_{max}(x, t) \simeq \sqrt{\frac{2c(1 - x)}{D} (t - t_{on})} \quad (11)$$

If L_{src} has kept constant over a long time, then $B_{\text{h}}(\phi)$ fades out at large ϕ because $\frac{d\sigma}{d\theta}$ drops at large θ . Therefore, while $\frac{d\sigma}{d\theta}$ shapes the radial brightness profile of the halo, x (or d_{sd} , if D is known) fully determines the halo size. Although a precise expression for $\frac{d\sigma}{d\theta}$ depends on the dust properties, we can approximate its 90% containment angle⁵³ as $\theta_{90} \simeq 0.3^\circ \times E_1^{-1}$ where $E = E_1$ keV is the photon energy. Since the lowest energy photons determine the size of the halo and 21 out of the 25 photons we used for our extension analysis have an energy $E > 1$ keV, we assume that $\theta_{90} \simeq 0.3^\circ$. After a time $t - t_{\text{on}} \simeq \frac{D}{2c}(1-x)\theta_{90}^2 \simeq 160 \text{ d} \times d_{10}$ the halo saturates to an angular size:

$$\phi_{\text{max}}(x, E) \simeq (1-x)\theta_{90}(E) \simeq 0.63 \text{ arcsec} \times d_{10} \quad (12)$$

As with the activation of the source, if L_{src} abruptly drops to 0 at an epoch t_{off} , then $B_{\text{h}}(\phi < \phi_{\text{min}}) = 0$ with:

$$\phi_{\text{min}}(x, t) \simeq \sqrt{\frac{2c(1-x)}{D}(t - t_{\text{off}})} \quad (13)$$

In this simple model we expect a sharp hole expanding in the halo starting from its center, without altering the profile of the halo for $\phi > \phi_{\text{min}}$. In a more realistic case, in which the source takes some time to switch off and light scatters in a smooth distribution of dust at various x , we expect a more complex halo profile and evolution.

As Swift monitoring shows that ULX1 remained in a high state ($L_{\text{on}} \simeq 10^{41} \text{ erg s}^{-1}$) for ~ 4 years^{54,55}, before switching off, we expect that the halo is complete, for any reasonable value of d_{sd} (up to ~ 90 kpc). We observed ULX1 switching off on 2017 July 10 (our t_{off}) and Chandra observation 20830 took place on 2017 November 7, 120 d later. Therefore, we expect a hole in the halo profile with a radius $\phi_{\text{min}} \simeq 0.54 \text{ arcsec} \times d_{10}^{1/2}$. As described in the extension analysis section, our fit to a halo profile estimates at the 90% confidence level that $d_{\text{sd}} = 11 \pm 5$ kpc.

We consider now the structure and geometry of NGC 5907 to constrain the location of ULX1 within its host galaxy. A model that accounts for optical emission and extinction⁵⁶ estimates the inclination of the galaxy plane as 87.2 ± 0.2 . A double exponential spatial model sets the scale length for dust and stars as $h_{\text{d}} = 8.2 \pm 0.2$ kpc, and $h_{\text{s}} = 7.2 \pm 0.1$ kpc, respectively. The dust radial profile shows a steep decrease at ~ 16 kpc, while the gas extends much further out⁵⁷. We approximate NGC 5907 to a perfectly thin edge-on galaxy and apply a simple geometrical model sketched, face-on, in Suppl. Fig. 6. The distance between ULX1 and a dust layer is d_{sd} , where r_{d} is the distance of the dust cloud from the center of NGC 5907, r_{s} is the distance of ULX1 from the center of NGC 5907, and $d_{\text{p}} = 8.3$ kpc is its sky projection. Given the constraints above, the optical depth is minimal when $r_{\text{d}} = 16$ kpc and $d_{\text{sd}} = 6$ kpc.

We follow a standard approach that assumes that the dust distribution, and therefore optical absorption, is a good proxy to track the metals that cause the X-ray absorption.⁵⁸ The numerical integration of a model describing the optical absorption in NGC 5907⁵⁹, along the line of sight up to ULX1, leads to $6.4 \text{ mag} < A_{\text{V}} < 12.6 \text{ mag}$. Assuming Solar abundances, we convert⁵⁸ these values into an estimate of the hydrogen column density: $1.4 \times 10^{22} \text{ cm}^{-2} < N_{\text{H}} < 2.8 \times 10^{22} \text{ cm}^{-2}$.

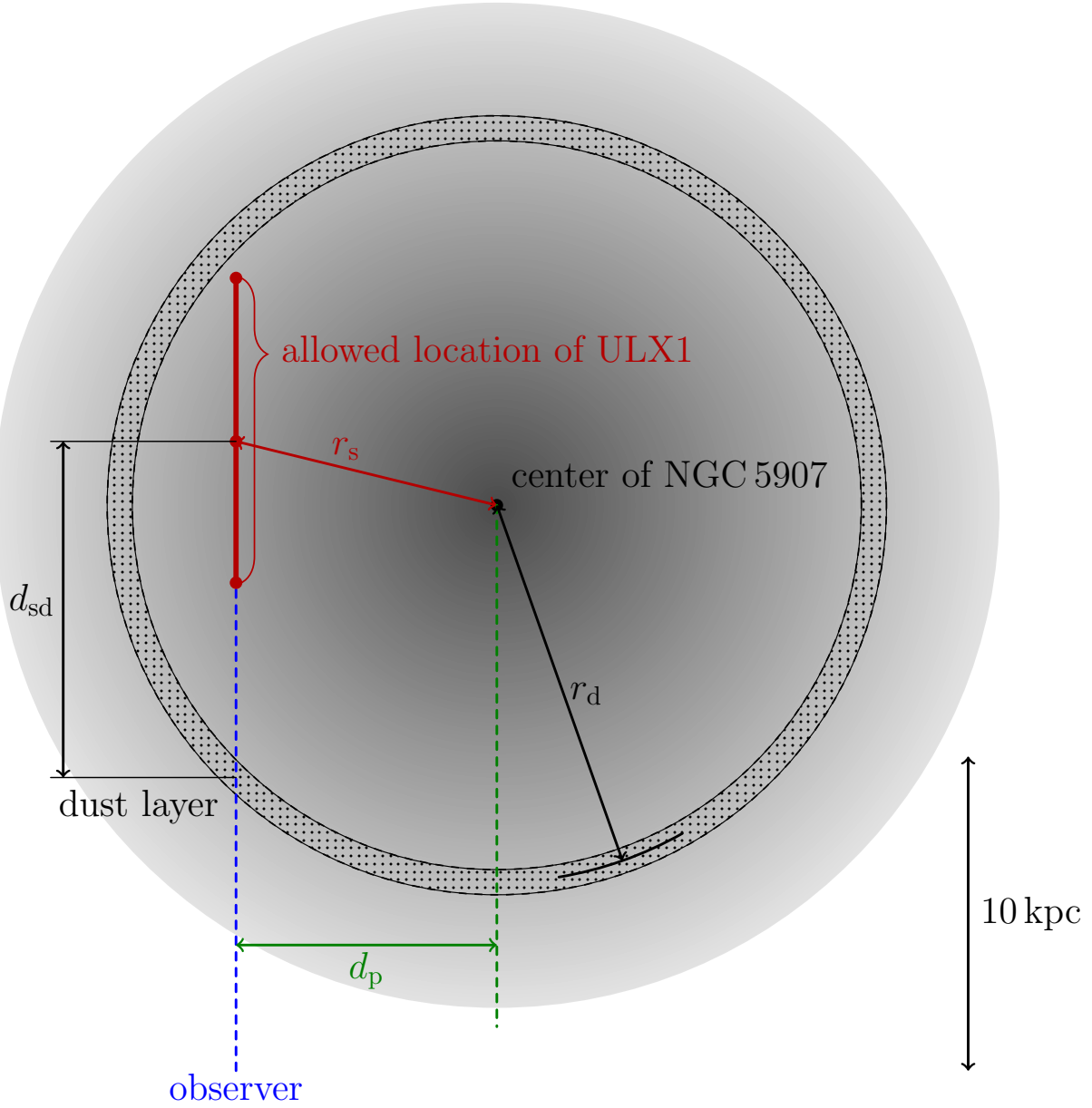


Figure 6: Schematic representation of NGC 5907 viewed face-on, and geometrical constraints provided by the dust-scattering scenario. The shaded grey region reproduces the radial dust distribution observed in NGC 5907.⁵⁶ If we assume that a dust wall is located at $r_d = 12$ kpc from the center of NGC 5907, then all distances are in scale, apart for the shape of the dust layer, here pictured as a thick ring, but whose global structure we ignore. The projected distance of ULX1 from the center of NGC 5907 is $d_p = 8.3$ kpc. The distance between the dust layer and ULX1 is constrained by the model to $d_{sd} = 11 \pm 5$ kpc. The thick vertical red line, along the blue dashed line of sight, marks the range of physical locations of ULX1 allowed by this model. The distance between ULX1 and the center of NGC 5907 is r_s . As the line of sight crosses a sizable portion of the plane of NGC 5907, optical and X-ray absorption should be very large.

This estimate is not consistent with the value of $N_{\text{H}} = 5.3 \times 10^{21} \text{ cm}^{-2}$ we see from ULX1 in its high state⁵⁵ (which includes absorption internal to the source). Uncertainties in the distribution and properties of the dust prevent us from drawing firm conclusions but, since the dust-scattering hypothesis seems to require some degree of fine tuning in the dust and galaxy parameters to reproduce the data, we do not further explore this scenario.

Multi-wavelength Coverage

The region around ULX1 has been observed in H_{α} with the 0.9 m telescope at the Kitt Peak National Observatory⁶⁰ and in radio at 5 GHz with the Very Large Array in configuration B⁶¹. The H_{α} image of NGC 5907 shows a large number of excesses on the order of a few $10^{-15} \text{ erg cm}^{-2} \text{ s}^{-1}$, that follow the profile of the galaxy. One of them, with a flux $F_{\alpha} \approx 9 \times 10^{-16} \text{ erg cm}^{-2} \text{ s}^{-1}$, is consistent with the direction of ULX1. However, the poor angular resolution (~ 1 arcsec) hampers a firm association with the X-ray nebula, or any further characterisation of the H_{α} feature. The radio observation reveals no point source down to a flux density of $20 \mu\text{Jy}$ within 10 arcsec around the direction of ULX1.

For a fully radiative strong collisional shock we expect that the flux in the Balmer lines is proportional to the mechanical power⁶² $L_{\text{m}} = \frac{12}{55} L_{\text{w}}$ and depends on the shock speed.^{63,64} Most of the recombination happens in the photoionized pre-shock region, or in the post-shock region where the plasma has already cooled. Because the age of the nebula is smaller than the cooling time of the plasma, we expect this contribution to be negligible.

The MAPPINGS III shock model library tables (http://cdsweb.u-strasbg.fr/~allen/mappings_page1.html) including both the pre- and post-shock regions, lead to an expected unabsorbed flux in H_{β} :

$$F_{\beta} = (1.53 \pm 0.20) \times 10^{-16} \text{ erg cm}^{-2} \text{ s}^{-1} \times \frac{L_{\text{w}}}{10^{40} \text{ erg s}^{-1}} \times d_{17}^{-\frac{1}{2}}$$

and an expected unabsorbed flux in H_{α} :

$$F_{\alpha} = (4.7 \pm 0.7) \times 10^{-16} \text{ erg cm}^{-2} \text{ s}^{-1} \times \frac{L_{\text{w}}}{10^{40} \text{ erg s}^{-1}} \times d_{17}^{-\frac{1}{2}}$$

This value, obtained under the assumption of a fully radiative strong shock, is in slight tension with the excess observed by the Kitt Peak National Observatory, if we adopt the estimate of L_{w} obtained in the adiabatic assumption, eq.6 in the main text. However, the strong optical absorption in the direction of ULX1⁶⁵ might reduce this tension.

The bremsstrahlung emissivity of a hot plasma at radio frequencies can be written⁶⁶ as:

$$j_{\nu} = \frac{8e^6}{3mc^2} \left(\frac{2\pi}{3mc^2} \right)^{\frac{1}{2}} (kT)^{-\frac{1}{2}} Z^2 n_i n_e \frac{\sqrt{3}}{\pi} \ln \left(\frac{4 kT}{\zeta h\nu} \right)$$

where $\zeta = 1.781\dots$ is the exponential Euler-Mascheroni constant. For pure hydrogen, with a compression factor $W \gtrsim 4$, we expect a radio flux density:

$$F_{5\text{GHz}} = 1.74 \times 10^{-3} \mu\text{Jy} \times \left(\frac{W}{4}\right) \times \left(\frac{n_{\text{ism}}}{\text{cm}^{-3}}\right)^2 \times \left(\frac{R}{112 \text{ pc}}\right)^3 \times \left(\frac{kT}{\text{keV}}\right)^{-\frac{1}{2}} \times \left(18.5 + \ln\left(\frac{T}{\text{keV}}\right)\right)$$

We expect no detectable radio emission from the hot X-ray-emitting plasma. Instead, under the assumption of a fully radiative strong shock, we expect some detectable radio emission from other regions.

If we combine the above estimate for F_β to the relation between the H_β and the 5 GHz emissivities⁶⁷ for a plasma with $k_B T = 1.9 \text{ keV}$, we obtain:

$$F_{5\text{GHz}} = 12.0 \mu\text{Jy} \times \frac{F_\beta}{10^{-16} \text{ erg cm}^{-2}\text{s}^{-1}} = 18.3 \pm 2.4 \mu\text{Jy} \times \frac{L_w}{10^{40} \text{ erg s}^{-1}} \times d_{17}^{-\frac{1}{2}}$$

VLA did observe at 5GHz NGC 5907 ULX-1 for 3h on May 30 2012, in the B configuration,⁶¹ reporting an upper limit of $20 \mu\text{Jy beam}^{-1}$. Because the beam width at half power for VLA at 5GHz in configuration B measures 1.2 arcsec, we expect that the bubble may be covered by a few beams, depending on the size of the radio nebula. Deriving a limit on the brightness of extended sources with an aperture synthesis array is a non-trivial task,⁶⁸ that goes beyond the scope of this paper.

The tension between our estimates and the reported upper limit indicates that a fully radiative shock approximation might not apply to our case. Indeed, such an approximation implies that all the mechanical power L_m is radiated, while, according to our model of the nebula, $L_{\text{bol}} \approx L_X \ll L_m$. Dropping the assumption of a fully radiative shock requires a more sophisticated and complete model of the nebula, that accounts for multiple plasma phases.

References

48. Walton, D. J., Roberts, T. P., Mateos, S. & Heard, V. 2XMM ultraluminous X-ray source candidates in nearby galaxies. *Mon. Not. R. Astron. Soc.* **416**, 1844–1861 (2011).
49. Predehl, P. & Schmitt, J. H. M. M. X-raying the interstellar medium: ROSAT observations of dust scattering halos. *Astron. Astrophys.* **293**, 889–905 (1995).
50. Vaughan, S. *et al.* The Discovery of an Evolving Dust-scattered X-Ray Halo around GRB 031203. *Astrophys. J.* **603**, L5–L8 (2004).
51. Vasilopoulos, G. & Petropoulou, M. The X-ray dust-scattered rings of the black hole low-mass binary V404 Cyg. *Mon. Not. R. Astron. Soc.* **455**, 4426–4441 (2016).
52. Mathis, J. S. & Lee, C.-W. X-ray halos as diagnostics of interstellar grains. *Astrophys. J.* **376**, 490–499 (1991).

53. Draine, B. T. Scattering by Interstellar Dust Grains. II. X-Rays. *Astrophys. J.* **598**, 1026–1037 (2003).
54. Walton, D. J. *et al.* A 78 Day X-Ray Period Detected from NGC 5907 ULX1 by Swift. *Astrophys. J.* **827**, L13 (2016).
55. Israel, G. L. *et al.* An accreting pulsar with extreme properties drives an ultraluminous x-ray source in NGC 5907. *Science* **355**, 817–819 (2017).
56. Xilouris, E. M., Byun, Y. I., Kylafis, N. D., Paleologou, E. V. & Papamastorakis, J. Are spiral galaxies optically thin or thick? *Astron. Astrophys.* **344**, 868–878 (1999).
57. Alton, P. B., Xilouris, E. M., Misiriotis, A., Dasyra, K. M. & Dumke, M. The emissivity of dust grains in spiral galaxies. *Astron. Astrophys.* **425**, 109–120 (2004).
58. Watson, D. The Galactic dust-to-metals ratio and metallicity using gamma-ray bursts. *Astron. Astrophys.* **533**, A16 (2011).
59. Just, A., Möllenhoff, C. & Borch, A. An evolutionary disc model of the edge-on galaxy NGC 5907. *Astron. Astrophys.* **459**, 703–716 (2006).
60. Rand, R. J. Diffuse Ionized Gas in Nine Edge-on Galaxies. *Astrophys. J.* **462**, 712 (1996).
61. Mezcua, M., Roberts, T. P., Sutton, A. D. & Lobanov, A. P. Radio observations of extreme ULXs: revealing the most powerful ULX radio nebula ever or the jet of an intermediate-mass black hole? *Mon. Not. R. Astron. Soc.* **436**, 3128–3134 (2013). 1309.5721.
62. Weaver, R., McCray, R., Castor, J., Shapiro, P. & Moore, R. Interstellar bubbles. II - Structure and evolution. *Astrophys. J.* **218**, 377–395 (1977).
63. Dopita, M. A. & Sutherland, R. S. Spectral Signatures of Fast Shocks. I. Low-Density Model Grid. *Astrophys. J. Suppl.* **102**, 161 (1996).
64. Allen, M. G., Groves, B. A., Dopita, M. A., Sutherland, R. S. & Kewley, L. J. The MAPPINGS III Library of Fast Radiative Shock Models. *Astrophys. J. Suppl.* **178**, 20–55 (2008).
65. Heida, M. *et al.* Searching for the Donor Stars of ULX Pulsars. *Astrophys. J.* **871**, 231 (2019).
66. Rybicki, G. B. & Lightman, A. P. *Radiative Processes in Astrophysics* (John Wiley & sons, Inc., 1986).
67. Caplan, J. & Deharveng, L. Extinction and reddening of H II regions in the Large Magellanic Cloud. *Astron. Astrophys.* **155**, 297–313 (1986).
68. Crane, P. C. & Napier, P. J. Sensitivity. In Perley, R. A., Schwab, F. R. & Bridle, A. H. (eds.) *Synthesis Imaging in Radio Astronomy*, *Astron. Soc. Pac. Conf. Series* (1989).

Acknowledgements This research is based on observations made with the Chandra X-ray Observatory and has made use of software provided by the Chandra X-ray Center (CXC) in the application packages CIAO, ChIPS, and Sherpa. This research also made use of data obtained with the Neil Gehrels Swift Observatory and XMM–Newton. Swift is a NASA mission with participation of the Italian Space Agency and the UK Space Agency. XMM–Newton is an ESA science mission with instruments and contributions directly funded by ESA Member States and NASA. A.B. is grateful to A. Fabian for an interesting discussion and to S. Covino for help in optical data reduction. A.B. and G.N. are supported by EXTraS, a project funded by the European Unions (EU) Seventh Framework Programme under grant agreement no. 607452. We acknowledge funding in the framework of the project ULTraS (ASI–INAF contract N.2017-14-H.0). M.M. acknowledges funding from ASI–INAF contract N.2015-023-R.0. D.J.W. acknowledges financial support from an STFC Ernest Rutherford Fellowship.